

<https://doi.org/10.1038/s43247-024-01989-1>

# The Amazonian mangrove systems accumulate and release dissolved neodymium and hafnium to the oceans

Check for updates

Antao Xu<sup>1,2</sup>✉, Ed Hathorne<sup>1</sup>, Michael Seidel<sup>3</sup>, Te Liu<sup>1,7</sup>, Nils E. Asp<sup>4</sup>, Andrea Koschinsky<sup>5</sup>, Thorsten Dittmar<sup>3,6</sup> & Martin Frank<sup>1</sup>

Mangroves are essential tropical ecosystems nurturing a wide range of marine biodiversity and counteracting global warming by sequestering atmospheric carbon dioxide. Hence, the export mechanisms and fluxes of particulate and dissolved organic carbon and trace elements from mangroves directly influence coastal productivity, the global carbon cycle and thus global climate, which are, however, not well constrained. Here we find consistent radiogenic neodymium and hafnium isotopic compositions of porewater, sedimentary iron-manganese oxyhydroxides and coastal seawater, suggesting that the Amazonian mangrove belt supplies trace elements through porewater discharge, dissolution of iron-manganese oxyhydroxides and their interactions with seawater. Together, these processes supply  $8.4 \times 10^6 \text{ g yr}^{-1}$  dissolved neodymium, equivalent to 64% of the total sources of neodymium to the Amazonian coastal seawater. Globally, mangrove systems along the continental margins contribute 6–9% of the net neodymium input to the ocean, which is similar to the contributions from atmospheric deposition. A contribution of this magnitude is potentially also the case for other trace elements, given the strong correlations between neodymium and iron (Pearson  $r = 0.92$ ), and manganese ( $r = 0.75$ ) concentrations across the entire river-ocean section, emphasizing the crucial role of mangrove system inputs in micro-nutrient cycling.

Tropical mangrove forests serve as crucial sinks of atmospheric  $\text{CO}_2$ <sup>1,2</sup> and as critical buffer zones between land and oceans by trapping substantial amounts of continental material, including trace metals and organic materials<sup>3–7</sup>. Mangrove-dominated ecosystems also act as biochemical reactors, in which processes such as the decomposition of organic matter within sediments<sup>8</sup> and the generation and export of vast quantities of nutrients, particulate and dissolved organic carbon,  $\text{CO}_2$  and  $\text{CH}_4$ , along with trace elements (TEs) take place<sup>9–13</sup>. Export fluxes of particulate organic carbon, dissolved organic carbon, and TEs to the coastal ocean from the mangroves directly affect carbon sequestration and the food webs of surface ecosystems in tropical coastal waters<sup>14</sup>. Meanwhile, within the mangrove systems, diverse material sources and complex processes interact, including anthropogenic emissions, riverine (dissolved and particulate) inputs, sediment dissolution and porewater discharge, as well as estuarine removal or release, and sediment-seawater-porewater interactions. These factors

challenge the accurate quantification of TE exports from mangroves and a comprehensive understanding of the role of mangrove systems in marine biogeochemical cycles.

Particle-reactive rare earth elements (REEs) and hafnium (Hf) provide insights into different elemental sources and geochemical processes such as sediment-water interactions, enabled by the distinct REE patterns of river water, seawater and sediments<sup>15–17</sup>. The relative enrichment or depletion of cerium compared to neighboring REEs (named Ce anomaly) can identify redox conditions due to the redox-sensitive nature of Ce, as a consequence of which oxidized Ce (IV) is more efficiently adsorbed to particles and removed from water<sup>18</sup>. A positive gadolinium (Gd) anomaly typically represents anthropogenic source contributions given that medical imaging and wastewater discharge is the major Gd source in modern rivers and coastal oceans<sup>19–21</sup>. In tropical mangrove estuaries in New Caledonia REE patterns have been used to suggest that mangrove sediments supply substantial

<sup>1</sup>GEOMAR Helmholtz Centre for Ocean Research Kiel, Kiel, Germany. <sup>2</sup>Institute of Environmental Physics, Universität Heidelberg, Heidelberg, Germany. <sup>3</sup>Institute for Chemistry and Biology of the Marine Environment (ICBM), Carl von Ossietzky Universität Oldenburg, Oldenburg, Germany. <sup>4</sup>Institute for Coastal Studies, Federal University of Pará, Bragança, Brazil. <sup>5</sup>School of Science, Constructor University, Bremen, Germany. <sup>6</sup>Helmholtz Institute for Functional Marine Biodiversity at Carl von Ossietzky Universität Oldenburg (HIFMB), Oldenburg, Germany. <sup>7</sup>Present address: School of Ocean and Earth Science, University of Southampton, Southampton, UK. ✉e-mail: [axu16@outlook.com](mailto:axu16@outlook.com)

amounts of dissolved REEs to estuarine waters<sup>22</sup>. Enrichments of the light REE (LREE) relative to the heavy REE (HREE) observed in mangrove sediments from several areas (e.g., Indian Sundarbans, Zhangjiang estuary, China and Jaguaripe estuary, Brazil) have been suggested to result from sources or processes like the weathering of crustal materials, preferential scavenging of LREE by flocculation matter or adsorption by sediments and preferential mobilization of HREE into dissolved form<sup>23–25</sup>. Complementing the information from REEs, radiogenic Nd and Hf isotopic compositions, expressed as  $\epsilon_{Nd}$  and  $\epsilon_{Hf}$ , respectively (defined in Methods) are sensitive tracers of the rock type and weathering of their continental sources<sup>26–28</sup>. The  $\epsilon_{Nd}$  and  $\epsilon_{Hf}$  signatures trace seawater-particle interactions at the continent-ocean interface through isotopic fingerprints in river water, seawater and particles<sup>29</sup>. Radiogenic Nd and Hf isotopes are also powerful tracers of the origin and mixing of water masses and serve as proxies for past changes in ocean circulation<sup>26,30–32</sup>. Mangrove forests located along the land-ocean interface act both as sinks for continental materials and as sources of nutrients and metals to the coastal oceans<sup>10,33</sup> and thus also as a potential source of dissolved Nd and Hf to the ocean. Indeed, in the coastal seawater off the Amazonian mangrove belt elevated concentrations of TEs have been observed and linked to groundwater inflow in previous studies<sup>34–36</sup>. However, the sources and processes controlling these TE concentrations within the mangroves and their impact on oceanic REE and Hf budgets remain largely unknown.

In this study, we analyzed REEs in coastal surface seawater, the Caeté River, brackish intertidal creek water, porewaters, and the iron-manganese (Fe-Mn) oxyhydroxide fraction of sediments in combination with  $\epsilon_{Nd}$  and  $\epsilon_{Hf}$  signatures of coastal seawater, porewater ( $\epsilon_{Nd}$  only) and coastal sediment. This dataset allows the evaluation of processes within mangroves on various spatial scales including coastal seawater mixing, Caeté River estuarine processes, porewater-seawater mixing, and sediment-porewater/seawater interactions. Evidence combining REEs,  $\epsilon_{Nd}$ , and  $\epsilon_{Hf}$  reveals that porewater and Fe or Fe-Mn oxyhydroxides supply substantial amounts of dissolved REEs and Hf to coastal seawater and control its  $\epsilon_{Nd}$  and  $\epsilon_{Hf}$  distributions.

## Results and Discussion

### Dissolved REE and Hf concentrations and radiogenic Nd and Hf isotope compositions in the coastal area off the mangrove belt

Across the coastal area off the Amazonian mangroves (Fig. 1), Nd and Hf concentrations ([Nd], [Hf]) in seawater averaged  $35.8 \pm 6.6$  pmol kg<sup>-1</sup> and  $0.8 \pm 0.1$  pmol kg<sup>-1</sup> (1 SD, standard deviation,  $n = 11$ ), respectively, with the maximum reaching 44.7 pmol kg<sup>-1</sup> for [Nd] and 1.0 pmol kg<sup>-1</sup> for [Hf] (Fig. 2a, b). These concentrations are higher than mean values ( $n = 2$ ) of 30.6 pmol kg<sup>-1</sup> for Nd and 0.6 pmol kg<sup>-1</sup> for Hf in the Amazon estuarine waters at similar salinities (Sal: 29 ~ 31)<sup>37</sup>. Increased concentrations were also observed for other TEs such as Fe, nickel (Ni), cobalt (Co), titanium (Ti), aluminium (Al), and zinc (Zn) in these seawaters<sup>34–36,38</sup>. These observations support the comparison between these metals and Nd and Hf, the isotopic compositions of which allow the tracing of source contributions that elevate their concentrations in coastal seawater.  $\epsilon_{Nd}$  and  $\epsilon_{Hf}$  signatures in coastal surface seawater were  $-17.3 \pm 0.3$  and  $-8.0 \pm 0.8$  (1 SD,  $n = 11$ ), respectively, and were thus much less radiogenic than those in upstream tropical western Atlantic seawater ( $\epsilon_{Nd}$ :  $-12.5$ ,  $\epsilon_{Hf}$ :  $-0.7$ )<sup>37,39</sup>. This documents that increases in dissolved [Nd] and [Hf] are coupled with large shifts of  $\epsilon_{Nd}$  and  $\epsilon_{Hf}$  values in the coastal seawater, suggesting a source enriched in Nd and Hf with highly unradiogenic isotopic signatures (Fig. 3). The substantial shifts in dissolved  $\epsilon_{Nd}$  and  $\epsilon_{Hf}$  cannot be attributed to the adjacent Amazon River and Pará River as their  $\epsilon_{Nd}$  and  $\epsilon_{Hf}$  signatures are much more radiogenic at  $-9.4$  ( $\epsilon_{Nd}$ ) and  $+1.8$  ( $\epsilon_{Hf}$ ) and  $-14.1$  ( $\epsilon_{Nd}$ ) and  $-4.1$  ( $\epsilon_{Hf}$ ), respectively<sup>37</sup>. Given the elevated TE concentrations observed in many mangrove-estuaries<sup>13,22,40,41</sup>, the nearby Amazonian mangrove system is considered the primary source responsible for these changes, likely including contributions from riverine inputs, partial dissolution of mangrove sediments, and porewater discharge<sup>33,42</sup>.

### Dissolved REE variability in the Amazonian mangrove ecosystems

In the Caeté River estuary, the river-ocean section is divided into three zones based on salinity levels and mangrove distributions: the fluvial zone (Sal:

0.2–3.7), the mangrove-fringed zone (Sal: 3.7–33.6), and the coastal marine zone (Sal: 33.6–35.9) (Fig. 1c)<sup>43</sup>. In the fluvial zone, the dissolved [Nd] of Caeté River freshwater (Sal: 0.2) ranged from 494 to 531 pmol kg<sup>-1</sup>. Along the salinity gradient, dissolved [Nd] decreased rapidly in the low-salinity zone (Sal < 8) due to salt-induced coagulation and precipitation of (nano) particles and colloids (NPCs)<sup>44,45</sup> (Fig. 4a). The maximum removal of 71.6% for Nd (Supplementary Table S1) was substantially lower than in the Amazon estuary (90.8%) and in the Pará estuary (95.0%), which may be related to higher dissolved organic matter (DOM) in the Caeté River. In the mid- to high-salinity zone, several distinctly elevated [Nd] values were observed with the largest spike reaching 395 pmol kg<sup>-1</sup>, higher than expected from conservative mixing between river water and coastal seawater (blue dashed line in Fig. 4a). Furthermore, in order to examine if coagulation and removal of Nd continued with increasing salinity or if Nd addition in the mid- to high-salinity zone occurs after initial removal, a second conservative mixing line (green dashed line in Fig. 4a) has been calculated between the water samples corresponding to mixing with the seawater endmember following the maximum removal (Supplementary Table S1). Interestingly, we observed higher [Nd] compared to the values expected from the second conservative mixing line for salinities of 10–33 in the mangrove-fringed zone. Strikingly, at salinities of 11 and 16, observed [Nd] reached 259 pmol kg<sup>-1</sup> and 395 pmol kg<sup>-1</sup>, which exceeded 120% and 300% of the expected values of 113 pmol kg<sup>-1</sup> and 98 pmol kg<sup>-1</sup> from the second conservative mixing lines, respectively (Fig. 4a). These marked additions of Nd require a major supply from a third endmember other than Caeté River freshwater and seawater, particularly considering the substantial Nd removal (71.6%) noted in the low-salinity zone. Furthermore, in the coastal marine zone (Sal > 34.6), [Nd] in seawater was  $54 \pm 8$  pmol kg<sup>-1</sup> (1 SD,  $n = 5$ ), much higher than observations in either the Amazon estuary of  $23 \pm 2$  pmol kg<sup>-1</sup> (1 SD,  $n = 4$ , Sal > 35.4) or the upstream tropical western Atlantic seawater of 15 pmol kg<sup>-1</sup> (Sal: 36.4)<sup>39</sup>, implying a substantial contribution from the additional source that impacts dissolved Nd distributions in mangrove-fringed and coastal marine zones. The weak correlations between [Nd] and fluorescent DOM (FDOM, Pearson Coefficient,  $r = 0.33$ ,  $P = 0.12$ ,  $n = 23$ ), as well as between [Nd] and dissolved organic carbon concentrations ( $r = 0.18$ ,  $P = 0.42$ ,  $n = 23$ ), indicate that the observed increases in [Nd] in the mid- to high-salinity zones were not directly associated with organic matter (Supplementary Fig. S1). Instead, this additional source appears to be strongly linked to Fe or Fe-Mn cycling. This is revealed by strong correlations between [Nd] and [Fe] ( $r = 0.92$ ,  $P < 0.01$ ,  $n = 23$ , Fig. 4a), and between [Nd] and [Mn] ( $r = 0.75$ ,  $P < 0.01$ ,  $n = 23$ , Supplementary Fig. S1) across the entire river-ocean section. Therefore, the zigzag variations of [Nd] and [Fe] in the mid- to high-salinity zone are likely not due to sampling biases or noisy background, but are instead attributed to mangrove contributions through Fe-Mn cycling (see below discussion).

In the intertidal creek water of Furo do Meio (Fig. 1d), [Nd] exhibited tidal shifts between increased values of  $163 \pm 104$  pmol kg<sup>-1</sup> (1 SD,  $n = 6$ ) during low tide and  $86 \pm 17$  pmol kg<sup>-1</sup> (1 SD,  $n = 7$ ) during high tide (Fig. 4b). This phenomenon was particularly prominent in the samples taken on the same day, when during low tide creek water was saline (Sal: 37.7) and reached peak [Nd] values of 392 pmol kg<sup>-1</sup>, whereas during high tide creek water was fresher (Sal: 34.2) and had a lower value of 72 pmol kg<sup>-1</sup>. The increases and tidal changes of [Nd] in creek water indicate that a source within the mangroves supplies Nd, which is observed especially during low tide. This source can neither be attributed to river supply as there is no fluvial freshwater input<sup>9,43</sup>, nor to organic matter inputs, given the lack of strong correlations between [Nd] and FDOM ( $r = 0.41$ ,  $P = 0.12$ ,  $n = 13$ ) and between [Nd] and dissolved organic carbon concentration ( $r = 0.37$ ,  $P = 0.42$ ,  $n = 13$ ) (Supplementary Fig. S1). Instead, this source is closely related to the porewater discharge driven by tidal pumping and associated with Fe or Fe-Mn cycling indicated by the observed tidal variations in salinity<sup>9,43</sup> and strong correlation between [Nd] and [Fe] ( $r = 0.76$ ,  $P < 0.01$ ,  $n = 13$ , Fig. 4b) and between [Nd] and [Mn] ( $r = 0.61$ ,  $P < 0.01$ ,  $n = 13$ , Supplementary Fig. S1) in saline tidal creek water, respectively. Additionally, it has been reported that the [Fe] and [Mn] in these mangrove porewaters

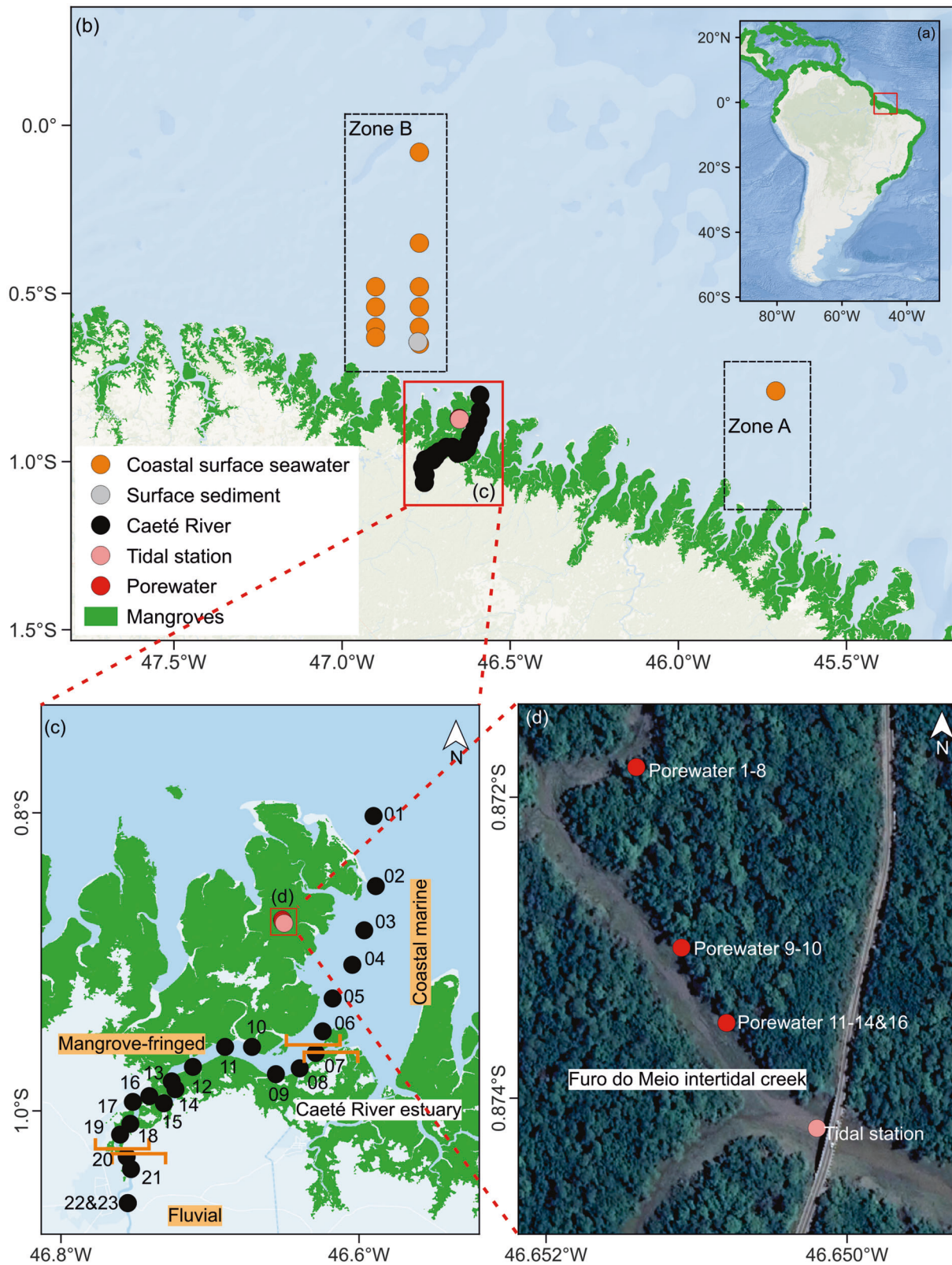


**Fig. 1 | Map of the study area showing sampling sites. a** View of the study area on the North Brazil continental shelf (red rectangle). **b** Sampling stations of coastal surface seawater (orange circles) and sediment (grey circles) in Zone A and B. The Amazonian mangrove area between Zone A and B covers 2200 km<sup>2</sup> along a coastline spanning 280 km. **c** Sampling sites across the Caeté River estuary (black circles) in

three sections (fluvial, mangrove-fringed, coastal marine) indicated by yellow brackets. **d** Sampling sites of intertidal creek water (pink circles) and porewater in the mangrove area (red circles). Mangrove coverage is marked by the green area in panels a, b and c. Source map from ©2020 Google Earth (Fig. 1d). Figures were generated by QGIS.

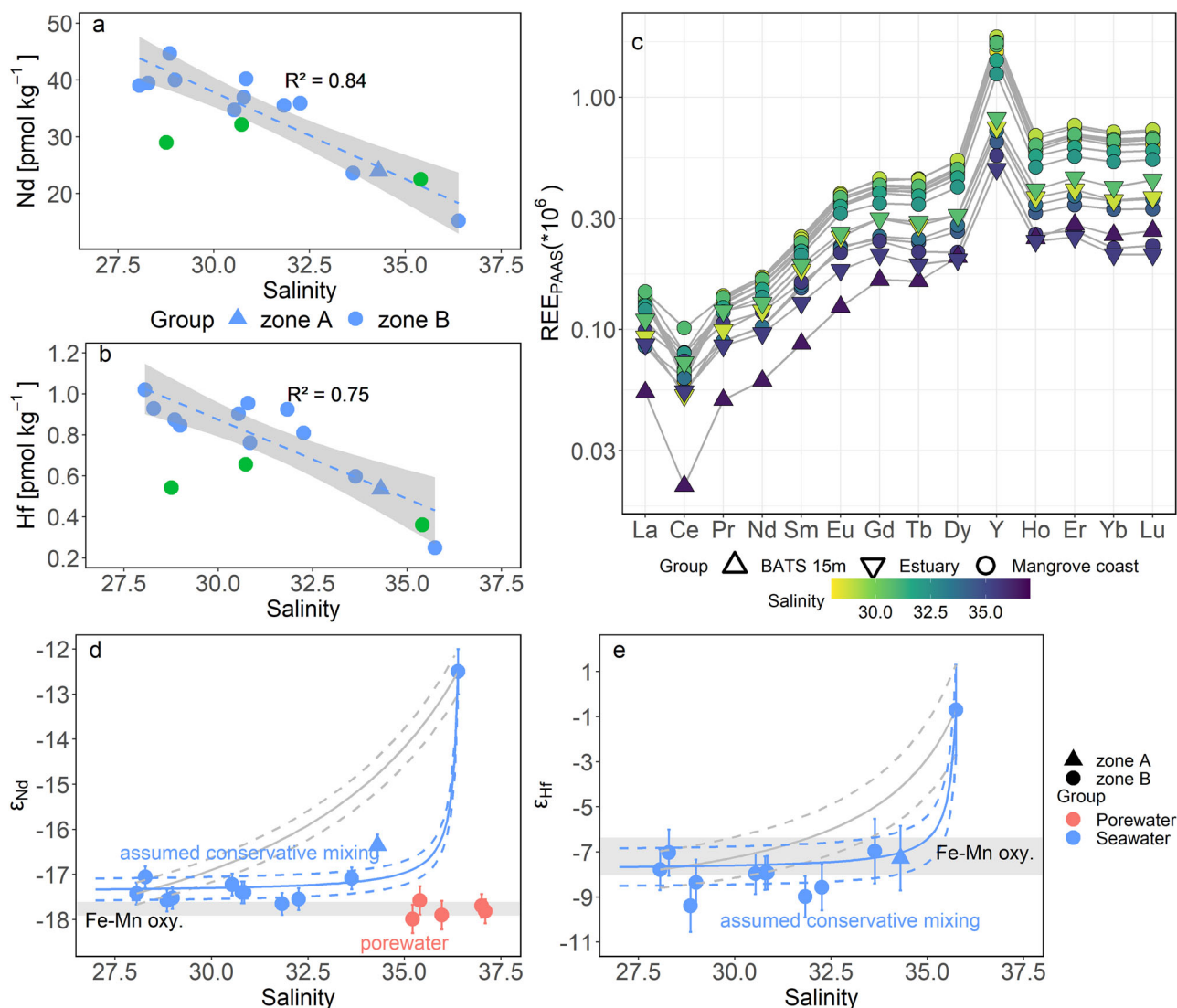


**Fig. 2 | Dissolved Nd and Hf concentrations ([Nd], [Hf]), rare earth element (REE) patterns,  $\epsilon_{Nd}$  and  $\epsilon_{Hf}$  distributions in the coastal area off the Amazonian mangrove belt. a, b** Dissolved [Nd] and [Hf] distributions versus salinity in coastal surface waters from zone A (blue rectangles) and zone B (blue dots). Data from Amazon estuarine waters are shown as green dots for comparison. Regression lines (blue dashed line) and 95% confidence intervals (CI, shaded gray area) in panels a and b are generated using data from the coastal area off the mangrove belt. **c** REE pattern of all coastal seawater stations across the mangrove-dominated coast (circles), Amazon estuarine water (rectangles) and the reference material (BATS 15 m, triangles) all normalized to PAAS (Post-Archean Australian Shale)<sup>90</sup>. Colors of the symbols represent salinity as indicated by the color bar. **d, e**  $\epsilon_{Nd}$  and  $\epsilon_{Hf}$  of coastal seawater (blue dots), porewater (pink dots) and labile Fe-Mn oxyhydroxides (gray

bars) versus salinity. Grey solid lines in panels d and e represent the two-endmember conservative mixing between the freshest coastal seawater (Sal: 28.1) and tropical western Atlantic seawater using measured [Nd] and [Hf] of these endmembers. Blue solid lines represent two-endmember (freshwater and seawater) conservative mixing using calculated [Nd] and [Hf] of the freshwater endmembers (4000 pmol kg<sup>-1</sup> and 50 pmol kg<sup>-1</sup>, respectively) assuming river supply as the sole dissolved source (Supplementary Fig. S2). Dissolved [Nd] or [Hf] and corresponding  $\epsilon_{Nd}$  or  $\epsilon_{Hf}$  signatures of tropical western Atlantic seawater are adopted from Zieringer<sup>39</sup> and are listed in Supplementary Table S2. The dashed lines above and below the corresponding solid lines reflect the uncertainties of the estimations of the  $\epsilon_{Nd}$  and  $\epsilon_{Hf}$  endmember values. Error bars correspond to 2 SD of the  $\epsilon_{Nd}$  and  $\epsilon_{Hf}$  measurements.

are  $87 \pm 72 \mu\text{mol L}^{-1}$  and  $26 \pm 16 \mu\text{mol L}^{-1}$ , respectively, which are several times higher than those in Caeté River freshwater, estuarine water and intertidal creek water, suggesting that porewaters can be major sources of Fe and Mn<sup>43</sup>.

Within the Amazonian mangroves, various processes are at play, including interactions between porewater, sediment and estuarine water/seawater, and the reductive dissolution of Fe(III) and/or Mn(IV) solid phases and TE release<sup>25,33</sup>. On top of this is a high porewater discharge of  $1.9 \times 10^4 \text{ m}^3 \text{ km}^{-2} \text{ day}^{-1}$  ( $\pm 5.1 \times 10^3$ , 1 SD), which is driven by tidal seawater pumping<sup>12</sup>. The REE patterns are useful for distinguishing different sources and processes enabled by the distinct patterns of river water, seawater, porewater and sediments<sup>15–17</sup> to help identify the dominating process responsible for [Nd] supply from mangroves. In the Caeté River estuary,

waters with elevated [Nd] exhibited a REE pattern characterized by a LREE increase without negative Ce anomalies (Fig. 4c), which was similar to those of porewaters and Fe-Mn oxyhydroxides (see below discussion). In the intertidal creek, the REE patterns of seawater during high tide and low tide were distinct (Fig. 4d). During high tide, the saline creek water displayed seawater-like LREE-depleted and HREE-enriched REE patterns with negative Ce anomalies (Fig. 4d). In contrast, during low tide, the REE patterns of creek water were characterized by increased LREE levels without negative Ce anomalies, suggesting a crustal-like LREE supply. Within the mangrove sediments, porewaters displayed remarkably high [Nd] ranging from 238 pmol kg<sup>-1</sup> to 4897 pmol kg<sup>-1</sup> with a mean value of  $2429 \pm 1892 \text{ pmol kg}^{-1}$  (1 SD,  $n = 8$ ). These porewaters showed two distinct REE patterns (Fig. 4e): i) an estuarine water-like pattern, characterized by a slight

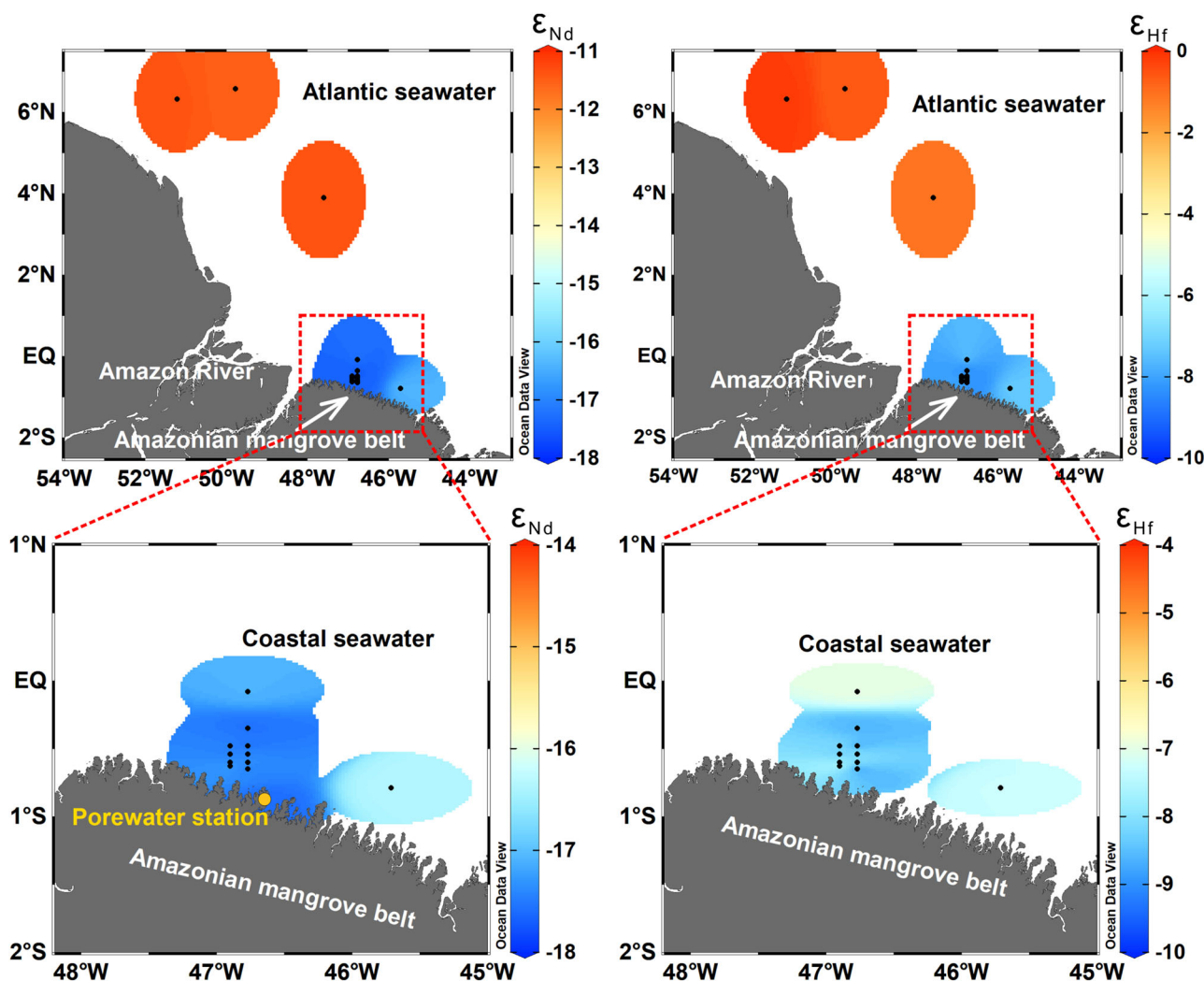


**Fig. 3 | Distributions of dissolved  $\epsilon_{Nd}$  and  $\epsilon_{Hf}$  in coastal surface seawater off the Amazonian mangrove belt.** Distinct  $\epsilon_{Nd}$  and  $\epsilon_{Hf}$  signatures in tropical western Atlantic seawater (orange) and coastal seawater off the Amazonian mangrove belt

(blue) suggest strong exchange/interaction between continental margins and coastal seawater along the Amazonian mangrove coast. Figures were produced using Ocean Data View (<https://odv.awi.de/>)<sup>91</sup>.

enrichment in HREE and a depletion in LREE without a Ce negative anomaly compared to estuarine water. This suggests the existence of a Ce supply to porewaters within reducing mangrove sediments enabling soluble Ce enrichment in porewaters<sup>46</sup>, and ii) a Fe-Mn oxyhydroxide-like pattern, being HREE-depleted and highly LREE enriched. Therefore, the elevated [Nd] and REE patterns of porewaters suggest that reductive dissolution of Fe-Mn oxyhydroxides is the main source elevating [REE] in porewater and shaping their REE patterns. This conclusion is also strongly supported by the consistent  $\epsilon_{Nd}$  signatures of the porewaters ( $-17.8 \pm 0.2$ , 1 SD,  $n = 5$ ) and the labile Fe-Mn oxyhydroxides in the sediments ( $-17.8 \pm 0.2$ ) (Table 1). Combining the evidence from Fe-Mn oxyhydroxide, porewater, estuarine water and tidal creek water data demonstrates that discharge from porewaters and interactions with labile Fe-Mn oxyhydroxides supply substantial amounts of REEs to Caeté River estuarine waters and tidal creek water within the Amazonian mangrove belt.

**Sources and processes controlling REE and Hf distributions in the coastal area**

We observed elevated [Nd] and [Hf] of coastal surface seawater with highly unradiogenic  $\epsilon_{Nd}$  and  $\epsilon_{Hf}$  signatures (Fig. 2 and Fig. 3). Potential sources along the mangrove-dominated coast that could supply Nd and Hf to surface waters include river water, porewater discharge, and Fe-Mn oxyhydroxide and silicate phase dissolution of mangrove sediments. Assuming

mixing between river and seawater, the [Nd] values of Caeté River water ( $\sim 550 \text{ pmol kg}^{-1}$ ) are too low to cause the observed unradiogenic  $\epsilon_{Nd}$  and  $\epsilon_{Hf}$  compositions of the surface waters (Fig. 2d, e and Supplementary Fig. S2). Hence, the Caeté River is likely not the sole source of REEs for coastal seawater. In consideration of the extremely high [Nd] in porewaters (up to  $4897 \text{ pmol kg}^{-1}$ ) and similar REE patterns of porewater, labile Fe-Mn oxyhydroxides, Caeté estuarine water, and creek tidal water (Fig. 4), porewater discharge and Fe-Mn oxyhydroxide dissolution were likely the main contributors of Nd to coastal seawater. This is supported by consistent  $\epsilon_{Nd}$  values among coastal seawater ( $-17.3 \pm 0.4$ , 1 SD,  $n = 11$ ), porewaters ( $-17.8 \pm 0.2$ , 1 SD,  $n = 5$ ), and Fe-Mn oxyhydroxides ( $-17.8 \pm 0.2$ ). It is challenging to unambiguously distinguish the influence of clay, silt, and residual bulk silicate sediment dissolution on coastal seawater based solely on the  $\epsilon_{Nd}$  signatures of the different solid phases given their narrow ranges ( $-17.0 \pm 0.1$ ,  $-19.2 \pm 0.1$ , and  $-18.8 \pm 0.1$ , respectively), which are similar to those of porewater and coastal seawater. The  $\epsilon_{Hf}$  signatures provide further insights into the contributions from different silicate phases as they are strongly influenced by mineral weathering<sup>47</sup>. The mean  $\epsilon_{Hf}$  signature of  $-8.0 \pm 0.8$  (1 SD,  $n = 11$ ) in coastal seawater is identical within error to the  $\epsilon_{Hf}$  signature of the Fe-Mn oxyhydroxide phases ( $-7.2 \pm 0.8$ ). In contrast, the  $\epsilon_{Hf}$  signatures of the clay, silt, and residual bulk silicate phases ( $-14.2 \pm 0.2$ ,  $-38.5 \pm 0.2$ , and  $-38.4 \pm 0.2$ , respectively) are all markedly less radiogenic than coastal seawater. The Hf isotopes thus clearly document that the

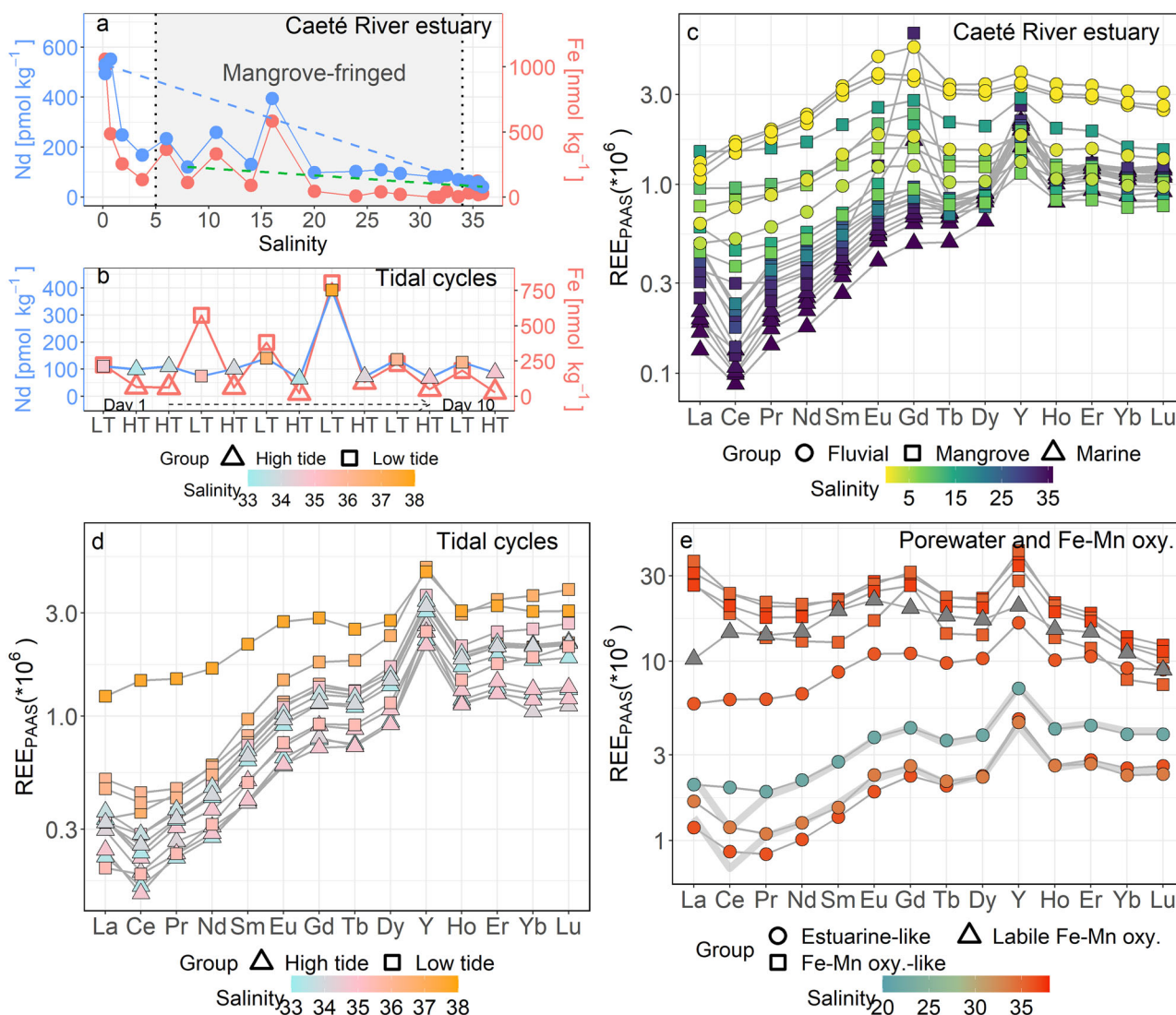


**Fig. 4 | Rare earth element (REE) patterns of waters from the Caeté River section, tidal station, and of porewater and sedimentary Fe-Mn oxyhydroxides.** **a** Distributions of Nd and Fe concentrations of Caeté River estuarine waters. The blue dashed line in panel a represents the calculated conservative Nd mixing line between the freshwater and seawater endmembers along the river transect. The second conservative mixing line (green dashed line) for Nd is defined by endmembers representing maximum Nd removal and seawater. **b** Distributions of Nd and Fe concentrations of intertidal creek water over 10 days of tidal cycles. Fe

concentrations are from Knoke et al.<sup>43</sup>. **c** REE patterns of Caeté River estuarine waters, **d** brackish intertidal creek water, **e** porewater and labile Fe-Mn oxyhydroxides coatings of sediment. Sample salinities are indicated by the color bar in each panel. All REE patterns are normalized to PAAS<sup>90</sup>. The REE pattern of labile Fe-Mn oxyhydroxides is scaled down by a factor of 1000 to facilitate comparison. The REE patterns of Caeté estuarine waters (Sal: 20, solid gray line) were added for comparison and magnified by factors of 3 and 5 in panel e.

isotopic signature of coastal seawater is controlled by the Fe-Mn oxyhydroxide phases with little influence of the residual silicate phases of the sediments.

To elucidate the contributions from the aforementioned sources (i.e., dissolved riverine input, porewater discharge, and labile Fe-Mn oxyhydroxide supply), we established a Nd mass balance model (Supplementary Figs. S3 and S4). Contributions from riverine input, porewater discharge, and labile Fe-Mn oxyhydroxide supply to the gross Nd flux (i.e., total Nd output from the mangrove system) amounted to  $56.9 \pm 2.1\%$ ,  $8.8 \pm 3.1\%$ , and  $34.3 \pm 4.4\%$ , respectively (Table 2). For the net Nd flux (i.e., the flux after dissolved Nd removal in the estuary and at the coast), the contribution of riverine input dropped to 36.0% after subtraction of the removal fluxes in the estuary and of the additional Nd inputs from the mangroves to the estuarine waters. Correspondingly, the contributions from porewater discharge and labile Fe-Mn oxyhydroxide dissolution together accounted for 64.0% of the total sources of dissolved Nd to the coastal waters (Table 2). These results suggest that porewater discharge, reductive dissolution of Fe or

Fe-Mn oxyhydroxides, and/or their interactions with coastal seawater are the primary drivers of the dissolved [Nd] and [Hf] as well as  $\epsilon_{Nd}$  and  $\epsilon_{Hf}$  distributions in coastal seawater, which is supported by the REE patterns and  $\epsilon_{Nd}$  and  $\epsilon_{Hf}$  data discussed above.

To clarify the processes controlling REE cycling within mangrove systems, a schematic figure (Fig. 5) is included. Mangroves produce and store large quantities of organic matter in the mangrove sediments with a global annual burial rate of  $2.6 \times 10^{13}$  g organic carbon<sup>48</sup>. Within the sediments, organic matter acts as a rich source of DOM, which binds and stabilizes REE in solution thereby preventing their precipitation and removal by NPCs<sup>49–51</sup>. The high abundance of organic matter in the Amazonian mangroves promotes the transport of dissolved REEs from the rivers to the coastal ocean, leading to a lower removal of [Nd] in the Caeté River estuary (71.6%) than in the Amazon River estuary (90.8%)<sup>37</sup>. Furthermore, increased microbial respiration and decomposition fueled by organic matter promotes the prevalence of anoxic conditions within the sediments and porewaters of the mangrove systems<sup>52</sup>. The occurrence of such anoxic

conditions facilitates the reductive dissolution of Fe-Mn oxyhydroxides<sup>53,54</sup>, thus creating a positive feedback leading to elevated dissolved [REE]. This is because tidal-driven porewater discharge and dissolution of Fe-Mn oxyhydroxides and/or interaction with seawater promotes the remobilization of REEs and their release to the water column. These processes ultimately control REE concentrations and  $\epsilon_{Nd}$  and  $\epsilon_{Hf}$  distributions in the coastal area. Nevertheless, REEs are removed from solution through scavenging during sediment resuspension by oxidized Fe and/or Mn phases (e.g., Fe and Mn sulfides)<sup>55</sup>, which are abundant in mangrove sediments<sup>25,56,57</sup>, and via flocculation and precipitation of Fe and Mn colloids during mixing of freshwater and seawater. Also, REEs, in particular LREE, are absorbed, mobilized, and partitioned within mangrove plants, and root activity may strongly influence their vertical distribution in core samples<sup>23</sup>. REE accumulation in Indian mangrove plants was found to be  $5 \text{ mg kg}^{-1}$ , accounting for 3.3% of total REE concentrations in the surrounding sediments<sup>23</sup>. Moreover, uptake of REEs by plants becomes more significant when sediment pH is low<sup>58</sup>. However, the concentration of REE in mangrove plants is relatively low compared to their abundance in bulk mangrove sediments, where Al and Fe oxy-hydroxides are the primary host phases<sup>25</sup>. Consequently, the dynamic redox cycles of Fe and Mn phases within mangrove systems play a pivotal role in controlling REE cycling in mangrove-dominated coastal areas, as evidenced by the strong correlations between [Nd] and [Fe] or [Mn] shown in Fig. 4.

### Implications for global oceanic trace element budgets and consequences of mangrove loss

Determination of the accurate oceanic budgets of Nd and Hf is essential to reliably apply Nd and Hf isotopes as tracers for identifying water mass sources and their mixing in the present-day ocean and as proxies for past variations in global ocean circulation. However, quantifying the oceanic Hf

**Table. 1 | Nd concentrations ([Nd]) and isotopic signatures ( $\epsilon_{Nd}$  and  $\epsilon_{Hf}$ ) in coastal seawater, porewater, labile Fe-Mn oxyhydroxide, clay, silt and residual sediment**

Sample	$\epsilon_{Nd}$ , SD	$\epsilon_{Hf}$ , SD	[Nd] (pmol kg <sup>-1</sup> )
Porewater 1 + 2	-17.6 ± 0.3	—	3044
Porewater 3 + 4	-18.0 ± 0.3	—	4897
Porewater 9 + 10	-17.8 ± 0.3	—	4154
Porewater 11 + 12	-17.7 ± 0.3	—	4746
Porewater 16	-17.9 ± 0.3	—	1547
Labile Fe-Mn oxyhydroxides	-17.8 ± 0.2	-7.2 ± 0.8	—
Clay fraction	-17.0 ± 0.1	-14.2 ± 0.2	—
Silt fraction	-19.2 ± 0.1	-38.5 ± 0.2	—
Residue	-18.8 ± 0.1	-38.4 ± 0.2	—
Coastal seawater (n = 11)	-17.3 ± 0.4	-8.0 ± 0.8	35.8 ± 6.6

Note. External reproducibility (2 SD) of the  $\epsilon_{Nd}$  and  $\epsilon_{Hf}$  measurements were determined by running secondary standard NIST 3135a and CGHF1. 1 SD of coastal seawater  $\epsilon_{Nd}$  and  $\epsilon_{Hf}$  data was calculated from 11 samples.

budget remains challenging due to the limited global data. In contrast, more information is available for Nd fluxes to/from the ocean allowing to better constrain the different sources. Even with the latest estimate of a global dissolved riverine Nd flux of  $1.5 \times 10^9 \text{ g yr}^{-1}$ <sup>137</sup>, models still identify a substantial global Nd input deficit ranging from  $4.0$  to  $7.5 \times 10^9 \text{ g yr}^{-1}$ , which is required to balance both [Nd] and  $\epsilon_{Nd}$  distributions in the global ocean<sup>59-62</sup>. Possible missing Nd sources include submarine groundwater discharge<sup>63</sup>, benthic sediment flux<sup>64</sup> and particle dissolution/particle-seawater interaction (i.e., boundary exchange processes)<sup>29</sup>. In view of the high Nd and Hf contributions from mangrove systems observed in our study, the Nd flux from mangrove system is calculated in order to address its contribution to the deficit.

Our mass balance estimation suggests that the mean gross Nd flux from the Amazonian mangrove systems ( $2200 \text{ km}^2$  between zone A and B in Fig. 1) is  $9.0 \pm 0.37 \times 10^7 \text{ g yr}^{-1}$  (1 SD), including riverine supply, and  $3.9 \pm 0.37 \times 10^7 \text{ g yr}^{-1}$  (1 SD) without it. The corresponding mean Nd removal fluxes are calculated as  $7.7 \pm 0.37 \times 10^7 \text{ g yr}^{-1}$  (1 SD) and  $3.1 \pm 0.37 \times 10^7 \text{ g yr}^{-1}$  (1 SD). Consequently, the net Nd flux from Amazonian mangrove systems is  $1.3 \times 10^7 \text{ g yr}^{-1}$ , including a river contribution and  $8.4 \times 10^6 \text{ g yr}^{-1}$  without it (Table 3). In addition, estimates using a seawater residence time method give results similar to the mass balance model (Supplementary Table S4). Extrapolating data from Amazonian mangroves to a global scale (applying a global mangrove area of  $1.4 \times 10^5 \text{ km}^2$ )<sup>65</sup>, the global total mangrove flux is estimated at  $2.4 \pm 0.23 \times 10^9 \text{ g yr}^{-1}$  (1 SD) for Nd if river contributions are excluded and we only consider fluxes released through porewater discharge and the dissolution of Fe-Mn oxyhydroxides and/or exchange with seawater. Therefore, after subtracting mean removal fluxes of  $1.9 \pm 0.23 \times 10^9 \text{ g yr}^{-1}$  (1 SD) the net Nd flux is calculated at  $5.2 \times 10^8 \text{ g yr}^{-1}$  (Table 3). The calculated Nd flux from global mangroves is thus higher than the estimated Nd flux from global dust ( $2 \sim 4 \times 10^8 \text{ g yr}^{-1}$ ) and accounts for 6 to 9% of the global Nd input to the oceans<sup>59-61</sup>.

It is noted that the annual Brazilian mangrove loss occurs at a rate of 0.05% while the loss rate is 0.13% or 0.16% globally, due to human activity<sup>66,67</sup>. The amount of sediment trapped and organic matter production by mangroves are consequently expected to decrease. Therefore, the TE fluxes from the mangrove system may also decrease as their cycling is dependent on the variability of redox conditions and the reductive dissolution and (re)precipitation of Fe or Fe-Mn oxyhydroxides in sediments. A schematic diagram (Supplementary Fig. S5) illustrates potential changes in TE fluxes (e.g., Nd), in response to mangrove degradation. Mangrove systems are known to function as net sinks of nutrients (e.g., nitrate) and thus protect coastal ecosystems from negative impacts of nutrient enrichment<sup>68,69</sup>, while also serving as net sources of nutrients (e.g., phosphate) and metals to support food webs and sustain coastal productivity<sup>9,70,71</sup>. However, under the climate change-driven pressures such as sea-level rise, saltwater intrusions and rainfall extremes, the biogeochemistry of TEs in mangrove systems has been observed to change, leading to elevated dissolved concentrations and fluxes of TEs like Fe, Mn, copper (Cu), and mercury (Hg)<sup>40,72-74</sup>, with Cu and Hg potentially accumulating through food webs and being toxic to aquatic life. Given the essential role of mangrove ecosystems in controlling nutrient and heavy metal dynamics in coastal environments by trapping terrestrial material and nutrients, supplying essential nitrogen, phosphorus and micronutrients to

**Table. 2 | Contributions of various sources to gross and net Nd fluxes exported from Amazonian mangrove systems**

	Total	Riverine input	Porewater discharge	Fe-Mn oxyhydroxide release
Gross Nd flux (g yr <sup>-1</sup> )	$9.0 \pm 0.33 \times 10^7$	$5.1 \times 10^7$	$7.9 \pm 2.7 \times 10^6$	$3.1 \pm 0.48 \times 10^7$
Contribution to total sources (%)		56.9 ± 2.1	8.8 ± 3.1	34.3 ± 4.4
Net Nd flux (g yr <sup>-1</sup> )	$1.3 \times 10^7$	$4.7 \times 10^6$	$8.4 \times 10^6$	
Contribution to total sources (%)		36.0	64.0	

Note. The gross Nd flux represents the total Nd output from all sources while the net Nd flux is calculated by subtracting the removal Nd flux. Details of the calculations are provided in the Supplementary Figure. S3, Figure. S4 and Table S3.

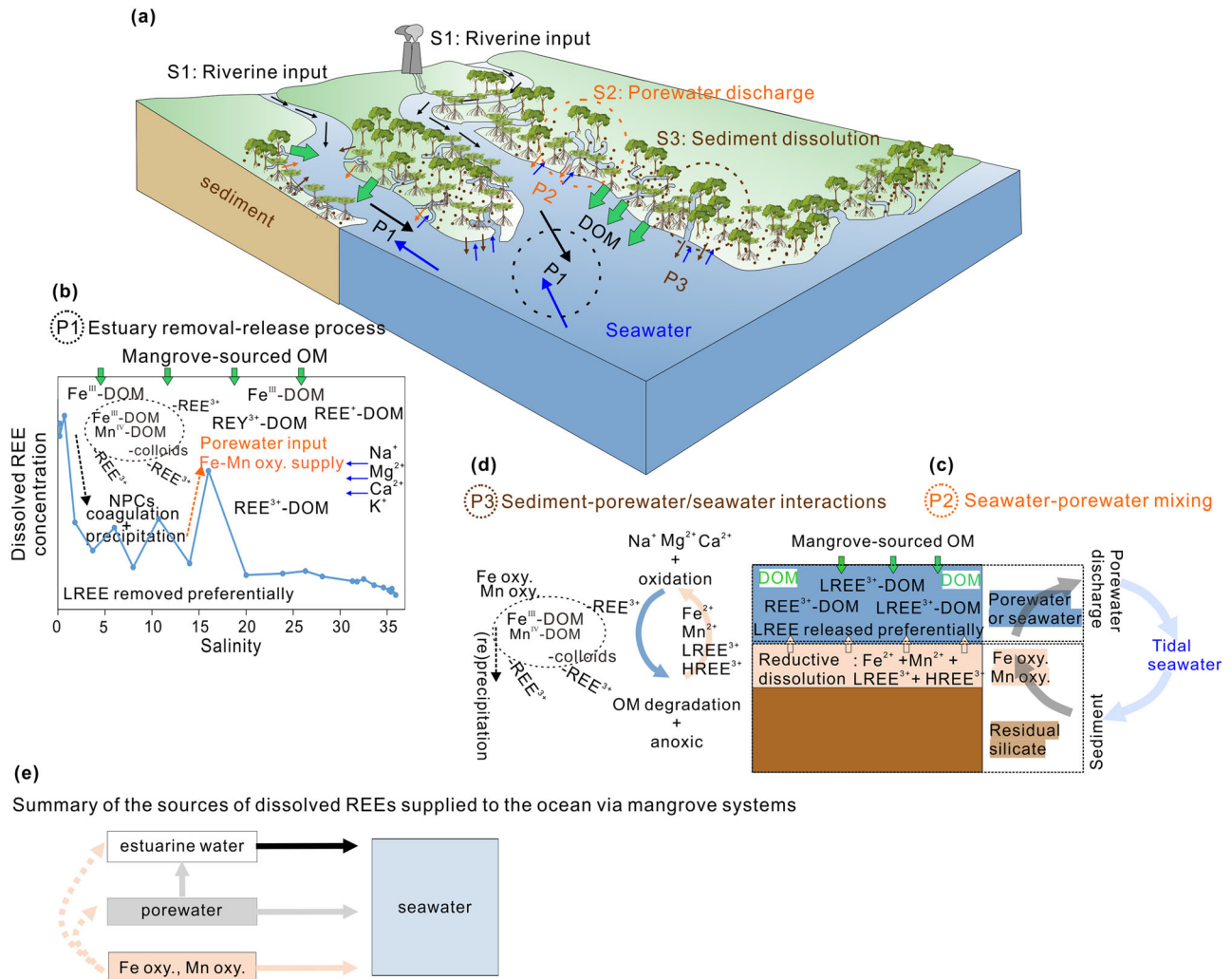


**Fig. 5 | Schematic representation of the rare earth element (REE) sources and cycling in mangroves and coastal areas.** **a** An overview of the sources and processes controlling REE dynamics in the mangroves and coastal areas. **b** REE removal-release processes in the estuary, including large-scale removal of dissolved REEs via salt-induced coagulation and precipitation of (nano-)particles and colloids (NPCs), along with porewater input and Fe-Mn oxyhydroxide dissolution supply elevating the [REE]. The presence of dissolved organic matter (DOM) exported from mangroves enhances the availability of dissolved REEs and prevents their removal from

solution. **c** Seawater-porewater mixing process in the mangrove areas. Porewater discharge is mainly driven by tidal seawater intrusion and retreat (pumping). **d** Sediment-porewater/seawater interactions. **e** Summary of the sources of dissolved REEs supplied to the ocean via mangrove systems. The schematic diagram highlights the variability of redox conditions regulating the reductive dissolution and (re) precipitation of Fe or Fe-Mn oxyhydroxides during porewater-seawater mixing and at the sediment-porewater-seawater interfaces, which subsequently impacts the REE cycles in the mangroves and the coastal areas.

**Table 3 | Calculated Nd fluxes from Amazonian and global mangrove systems**

	With riverine supply Mean, 1 SD, 1SE, 95% CI	Without riverine supply Mean, 1 SD, 1SE, 95% CI
Mean gross flux from Amazonian mangroves ( $\times 10^7$ g yr <sup>-1</sup> )	9.0, 0.37, 0.16, [8.7, 9.4]	3.9, 0.37, 0.16, [3.5, 4.3]
Mean removal flux ( $\times 10^7$ g yr <sup>-1</sup> )	7.7, 0.37, 0.16, [7.3, 8.1]	3.1, 0.37, 0.16, [2.7, 3.4]
Removal percentage (%)	85.5, 0.6, 0.3, [84.9, 86.1]	78.4, 2.1, 1.0, [76.2, 80.6]
Net flux from Amazonian mangrove ( $\times 10^7$ g yr <sup>-1</sup> )	1.3	0.84
Mean gross flux from global mangrove ( $\times 10^9$ g yr <sup>-1</sup> )	5.7, 0.23, 0.10, [5.4, 5.9]	2.4, 0.23, 0.10, [2.2, 2.7]
Mean global removal flux ( $\times 10^9$ g yr <sup>-1</sup> )	4.8, 0.23, 0.10, [4.6, 5.1]	1.9, 0.23, 0.10, [1.7, 2.2]
Net flux from global mangrove ( $\times 10^9$ g yr <sup>-1</sup> )	8.2	5.2

Note. The term “Amazonian mangroves” here refers specifically to the mangrove area between the zone A and zone B covering approximately 2200 km<sup>2</sup>. The gross Nd flux is the total dissolved Nd output from the Amazonian mangroves, comprising both the removal and net Nd fluxes. To calculate the Nd flux from the Amazonian mangrove system without the contribution from rivers, the Nd flux supplied by rivers has been subtracted using freshwater discharge and dissolved [Nd] with a maximum Nd removal of 90.8%, which is assumed to be the same as that of the Amazon River<sup>37</sup>. The standard deviation (1SD), standard error (1SE) and 95% confidence interval (CI) of the calculations are listed. The parameters and specific details used in the calculations are provided in the Supplementary Figure. S3, Figure. S4 and Table S3.

aquatic food webs, as well as their contribution to CO<sub>2</sub> sequestration, it is urgent to promote mangrove conservation.

Our study reports high Nd fluxes to the ocean from mangrove systems via dissolved riverine input, porewater discharge, and reductive dissolution of Fe-Mn oxyhydroxides and/or interactions with coastal seawater. Yet, these fluxes have not been included in global budgets and model applications. On a global scale, mangrove systems may supply a Nd flux of  $5.2 \times 10^8 \text{ g yr}^{-1}$ , which is similar to or even higher than that estimated for atmospheric deposition. Although our extrapolated global fluxes may have uncertainties due to limited sample stations during a single season in coastal mangrove areas, our study aligns with previous work in New Caledonia mangroves and highlights the role of mangrove systems in supplying TEs to coastal seawater. Overall, considering the biological functions of other TEs such as Fe, Mn, Zn, and Co in surface ocean ecosystems<sup>75</sup>, and the potential for substantial export of these elements from mangrove systems to coastal seawater, our findings emphasize the importance of acquiring a comprehensive understanding of the magnitude and impact of TE inputs originating from mangrove systems as well as the influence of mangrove loss on TE export. This understanding is crucial for effectively evaluating coastal ecosystem dynamics and their responses to environmental changes.

## Methods

### Sample collection and treatment

We sampled surface seawater ( $n = 11$ ) and surface sediment ( $n = 1$ ) off the Amazonian mangrove area on the continental shelf, water samples ( $n = 23$ ) along the entire salinity gradient (0 to >35) in the Caeté River estuary, tidal water samples ( $n = 11$ ) in the Furo do Meio intertidal creek (Sal: 33.3 ~ 37.7) and porewaters at eight different locations in the mangroves next to the creek (Fig. 1). Surface seawater samples were collected with a Conductivity-Temperature-Depth (CTD) rosette at 2 to 4 m water depth and surface sediment was obtained by a multiple corer during *RV Meteor* cruise M147 during the wet season (29 April to 20 May 2018, official process study GApr11 of the international GEOTRACES program). Samples were filtered through 0.45 μm Nucleopore filters within a few hours after collection and were acidified on board to pH ~2 using concentrated ultrapure distilled HCl. Surface waters (depth <2 m) in the Caeté River estuary were collected during the dry season (10th October) in 2017. The tidal seawater was sampled during high and low tide between the 27th September and 07th October, covering 11 tidal cycles from neap to spring tide, at depths of less than 0.5 m with a bucket that had been pre-rinsed three times with the sample. For porewater sampling, a small hole was dug in the sediment and five liters of porewater were obtained after discarding the initial two fillings of the accumulating water. These samples were filtered through 0.45 μm surfactant-free cellulose acetate (SFCA) syringe filters and were then acidified with ultrapure HNO<sub>3</sub> to reach a final concentration of 1% (v/v). More sampling details were reported in Knoke et al.<sup>43</sup>.

### Fe-Mn oxyhydroxide extraction and alkaline fusion

Approximately 1 g of sediment was treated with >18.2 MΩ grade deionized water for three times to remove any exchangeable ions<sup>76</sup>. Carbonate was removed using an Na acetate solution buffered to pH 4 with acetic acid (Merck Suprapur<sup>®</sup>) following Gutjahr et al.<sup>77</sup>. After centrifugation and decanting of the supernatant, sediment sample was triple rinses in >18.2 MΩ water. The labile Fe-Mn oxyhydroxide fraction was extracted by a diluted reductive solution (0.005 M hydroxylamine hydrochloride/1.5% acetic acid/0.03 M Na-EDTA solution buffered to pH 4 with NaOH) for 10 min following Huang et al.<sup>76</sup>. The sediment was then treated with a strong reductive solution (0.05 M hydroxylamine hydrochloride/15% acetic acid/0.03 M Na-EDTA solution buffered to pH 4 with NaOH) overnight to completely remove residual Fe-Mn oxyhydroxides following Gutjahr et al.<sup>77</sup>. In this study, the term “labile Fe-Mn oxyhydroxide phase” and “residual Fe-Mn oxyhydroxide phase” refer to the fractions extracted by the diluted and strong reductive solutions, respectively. The labile phase is considered more likely to dissolve and release TEs into the water, and is sensitive to pH and redox conditions<sup>78</sup>. The residual sediment samples were then separated into

clay and silt fractions following the method of Bretschneider et al.<sup>79</sup>. Both clay and silt parts were dried and homogenized prior to alkaline fusion following Bayon et al.<sup>80</sup>. The accuracy and reproducibility of the leaching experiment and fusion technique were monitored by processing reference materials with each batch of samples including marine sediment MESS-2 ( $n = 3$ ), USGS reference material BHVO-2 ( $n = 3$ ) and AGV-2 ( $n = 3$ ), and sample replicates ( $n = 3$ ), as shown in Supplementary Data.

### Neodymium and hafnium isotope analyses

Coastal surface seawater and porewater samples for  $\epsilon_{\text{Nd}}$  and/or  $\epsilon_{\text{Hf}}$  analysis were preconcentrated by Fe co-precipitation, followed by treatment with pre-cleaned di-ethyl ether to remove most of added Fe<sup>31</sup>. The REE and Hf were separated from matrix elements using cation exchange chromatography (AG<sup>®</sup> 50W-X8, 1.4 mL, 200–400 μm) according to the method described by Stichel et al.<sup>31</sup>. Nd and Hf were further purified for isotope measurements using Eichrom<sup>®</sup> LN-Spec resin (2 mL, 50–100 μm) following Pin and Zalduegui<sup>81</sup> and Bio-Rad AG<sup>®</sup> 1-X8 resin (2 mL, 200–400 μm) following the procedure by Münker et al.<sup>82</sup>, respectively. The <sup>143</sup>Nd/<sup>144</sup>Nd ratios were measured on a Neptune Plus MC-ICP-MS at GEOMAR and were corrected for instrumental mass bias to <sup>146</sup>Nd/<sup>144</sup>Nd = 0.7219 and to <sup>142</sup>Nd/<sup>144</sup>Nd = 1.141876 following the approach of Vance and Thirlwall<sup>83</sup>. The <sup>143</sup>Nd/<sup>144</sup>Nd ratios of all samples were normalized to the accepted values of the JNdi-1 standard value (0.512115)<sup>84</sup>. The <sup>176</sup>Hf/<sup>177</sup>Hf ratios measured on the Neptune Plus MC-ICPMS were corrected for instrumental mass bias to <sup>179</sup>Hf/<sup>177</sup>Hf = 0.7325 applying an exponential mass fractionation law. The standard Hf JMC 475 values were within uncertainty of the accepted value of 0.28216<sup>85</sup>. Total procedural blanks were below 30 pg for Nd and 28 pg for Hf and hence negligible ( $n = 5$ ). To ensure accuracy and external reproducibility, secondary standard solution NIST 3135a Nd, internal laboratory standard solution (CGHF1 Hf, Inorganic Ventures<sup>®</sup>) and USGS reference material NOD-A-1 were run with water samples and USGS reference materials AGV-2 and BHVO-2 were run with sediment samples. The external reproducibility of the Nd and Hf isotope measurements of water samples was determined using standard solutions with concentrations matching those of the measured samples in the range of 0.24–0.32  $\epsilon_{\text{Nd}}$  units (2 standard deviation, 2 SD) and 0.74–1.43  $\epsilon_{\text{Hf}}$  units (2 SD), respectively. For sediment samples, the reproducibility ranges were 0.08–0.15 units (2 SD) for Nd isotopes and 0.20–0.83 units (2 SD) for Hf isotopes. The reproducibility of measured Nd and Hf isotopic compositions in all figures is illustrated using the 2 SD values of the secondary standards NIST 3135a and CGHF1, as shown in Supplementary Data.  $\epsilon_{\text{Nd}}$  and  $\epsilon_{\text{Hf}}$  are defined by the Eqs. (1) and (2), respectively:

$$\epsilon_{\text{Nd}} = \left( \frac{(^{143}\text{Nd}/^{144}\text{Nd})_{\text{sample}}}{(^{143}\text{Nd}/^{144}\text{Nd})_{\text{CHUR}}} - 1 \right) \times 10^4 \quad (1)$$

$$\epsilon_{\text{Hf}} = \left( \frac{(^{176}\text{Hf}/^{177}\text{Hf})_{\text{sample}}}{(^{176}\text{Hf}/^{177}\text{Hf})_{\text{CHUR}}} - 1 \right) \times 10^4 \quad (2)$$

where the <sup>143</sup>Nd/<sup>144</sup>Nd and <sup>176</sup>Hf/<sup>177</sup>Hf ratios of CHUR (Chondritic Uniform Reservoir) are 0.512638<sup>86</sup> and 0.282785<sup>87</sup>, respectively.

### Neodymium and hafnium concentration analyses

1 L seawater samples were spiked with pre-weighed <sup>150</sup>Nd and <sup>180</sup>Hf spikes and preconcentrated using iron coprecipitation for Nd and Hf concentration measurements. The samples were then purified on a AG<sup>®</sup> 50W-X8 column following the method detailed in Rahlf et al.<sup>88</sup>. Hf cuts were further purified using AG<sup>®</sup> 1-X8 resin (1.6 mL, 200–400 μm) following Sahoo et al.<sup>89</sup>. The concentrations were calculated based on the <sup>150</sup>Nd/<sup>144</sup>Nd and <sup>178</sup>Hf/<sup>180</sup>Hf ratios obtained from a Nu Plasma MC-ICP-MS with an Aridus 2 desolvating nebulizer. The relative standard deviation (2RSD) was better than 0.6% for Nd and better than 1.2% for Hf according to repeated spiking, treatment and measurement one sample ( $n = 5$ ).

### Rare earth element and yttrium concentration analyses

The [REE] of water samples were pre-concentrated offline using a SeaFAST system (model M5 from Elemental Scientific) and analyzed on a Thermo Element XR ICP-MS coupled with a CETAC “Aridus 2” desolvating nebulizer at GEOMAR. Natural river and estuarine water reference materials (NRCC SLRS-6 and SLEW-3) and GEOTRACES inter-calibration samples BATS 15 m and 2000 m were pre-concentrated and measured together to monitor external reproducibility and accuracy. The oxide formation was monitored with element solutions of barium (Ba), Ce, praseodymium (Pr) + Nd, and samarium (Sm) + Eu + Gd + terbium (Tb) at the start of each analytical session. Oxide formation was <0.0002% for Ba, <0.04% for Ce, <0.03% for Pr+Nd and <0.05% for the MREE.

The mean values obtained for the reference waters are given in Supplementary Data. The [REE] of labile Fe–Mn oxyhydroxide, clay and silt parts of residue were measured on an Agilent 7500ce Quadrupole-ICP-MS at GEOMAR. The [REE] of bulk residue is calculated as the sum of the concentrations of the clay and silt components. The reproducibility was monitored by repeated measurements of one sediment sample, and USGS reference materials AGV-2 and BHVO-2. Mean values and 2 SD for the reference material measurements are given in Supplementary Data. Ce anomaly ( $Ce/Ce^*$ ), Gd anomaly ( $Gd/Gd^*$ ) and Eu anomaly ( $Eu/Eu^*$ ) are defined by Eqs. (3), (4) and (5), respectively:

$$Ce/Ce^* = \frac{3 * Ce_{PAAS}}{2 * La_{PAAS} + Nd_{PAAS} +} \quad (3)$$

$$Gd/Gd^* = \frac{3 * Gd_{PAAS}}{Sm_{PAAS} + 2 * Tb_{PAAS}} \quad (4)$$

$$Eu/Eu^* = \frac{3 * Eu_{PAAS}}{2 * Sm_{PAAS} + Tb_{PAAS}} \quad (5)$$

where Gd, Eu, samarium (Sm) and terbium (Tb) are Post-Archean Australian Shale (PAAS) normalized.

### Nd removal calculations in the Caeté River estuary

The percentage of Nd removal was quantified with Eq. (6):

$$\% \text{removal} = 1 - \frac{[Nd]_{\text{measured}}}{[Nd]_{\text{conservative}}} \times 100 \quad (6)$$

where  $[Nd]_{\text{measured}}$  represents measured concentrations and  $[Nd]_{\text{conservative}}$  represents concentrations expected from two-endmember conservative mixing for the same salinity.

### Reporting summary

Further information on research design is available in the Nature Portfolio Reporting Summary linked to this article.

### Data availability

All data generated in this study are provided in the Supplementary files and are also available on [PANGAEA](#).

Received: 18 April 2024; Accepted: 30 December 2024;

Published online: 08 January 2025

### References

- Twilley, R. R., Chen, R. H. & Hargis, T. Carbon sinks in mangroves and their implications to carbon budget of tropical coastal ecosystems. *Water Air Soil Pollut.* **64**, 265–288 (1992).
- Bouillon, S. et al. Mangrove production and carbon sinks: A revision of global budget estimates. *Glob. Biogeochem. Cycles* **22**, GB2013 (2008).
- Furukawa, K. & Wolanski, E. Sedimentation in mangrove forests. *Mangroves Salt Marshes* **1**, 3–10 (1996).
- Nittrouer, C. A. et al. Amazon Sediment Transport and Accumulation Along the Continuum of Mixed Fluvial and Marine Processes. *Ann. Rev. Mar. Sci.* **13**, 501–536 (2021).
- Lacerda Ld et al. The fate of trace metals in suspended matter in a mangrove creek during a tidal cycle. *Sci. Total Environ.* **75**, 169–180 (1988).
- Zhang, Z. W. et al. Heavy metal and organic contaminants in mangrove ecosystems of China: a review. *Environ. Sci. Pollut. Res Int* **21**, 11938–11950 (2014).
- De Lacerda, L. D. & Abrao, J. J. Heavy metal accumulation by mangrove and saltmarsh intertidal sediments. *Rev. Bras. Biol.* **7**, 49–52 (1984).
- Ramos Silva, C. A., da Silva, A. P. & de Oliveira, S. R. Concentration, stock and transport rate of heavy metals in a tropical red mangrove, Natal, Brazil. *Mar. Chem.* **99**, 2–11 (2006).
- Dittmar, T. & Lara, R. J. Do mangroves rather than rivers provide nutrients to coastal environments south of the Amazon River? Evidence from long-term flux measurements. *Mar. Ecol.-Prog. Ser.* **213**, 67–77 (2001).
- Dittmar, T., Hertkorn, N., Kattner, G. & Lara, R. J. Mangroves, a major source of dissolved organic carbon to the oceans. *Glob. Biogeochem. Cycles* **20**, GB1012 (2006).
- Call, M. et al. High pore-water derived CO<sub>2</sub> and CH<sub>4</sub> emissions from a macro-tidal mangrove creek in the Amazon region. *Geochim Cosmochim. Acta* **247**, 106–120 (2019).
- Cabral, A. et al. Carbon and alkalinity outwelling across the groundwater-creek-shelf continuum off Amazonian mangroves. *Limnol. Oceanogr. Lett.* **6**, 369–378 (2021).
- Mori, C. et al. Non-conservative Behavior of Dissolved Organic Matter and Trace Metals (Mn, Fe, Ba) Driven by Porewater Exchange in a Subtropical Mangrove-Estuary. *Front. Mar. Sci.* **6**, 481 (2019).
- Santos, I. R. et al. The renaissance of Odum’s outwelling hypothesis in ‘Blue Carbon’ science. *Estuar., Coast. Shelf Sci.* **255**, 107361 (2021).
- Zheng, X.-Y., Plancherel, Y., Saito, M. A., Scott, P. M. & Henderson, G. M. Rare earth elements (REEs) in the tropical South Atlantic and quantitative deconvolution of their non-conservative behavior. *Geochim Cosmochim. Acta* **177**, 217–237 (2016).
- Goldstein, S. J. & Jacobsen, S. B. Rare earth elements in river waters. *Earth Planet Sci. Lett.* **89**, 35–47 (1988).
- Hathorne, E. C., Stichel, T., Brück, B. & Frank, M. Rare earth element distribution in the Atlantic sector of the Southern Ocean: The balance between particle scavenging and vertical supply. *Mar. Chem.* **177**, 157–171 (2015).
- Elderfield, H. & Greaves, M. J. The rare earth elements in seawater. *Nature* **296**, 214–219 (1982).
- Rabiet, M., Brissaud, F., Seidel, J. L., Pistre, S. & Elbaz-Poulichet, F. Positive gadolinium anomalies in wastewater treatment plant effluents and aquatic environment in the Hérault watershed (South France). *Chemosphere* **75**, 1057–1064 (2009).
- Bau, M. & Dulski, P. Anthropogenic origin of positive gadolinium anomalies in river waters. *Earth Planet Sci. Lett.* **143**, 245–255 (1996).
- Speidel, L. G. et al. Rivers and tidal flats as sources of dissolved organic matter and trace metals in the German Bight (North Sea). *Biogeochemistry* **167**, 225–250 (2024).
- Dang, D. H. et al. Tropical mangrove forests as a source of dissolved rare earth elements and yttrium to the ocean. *Chem. Geol.* **576**, 120278 (2021).
- Mandal, S. K. et al. State of rare earth elements in the sediment and their bioaccumulation by mangroves: a case study in pristine islands of Indian Sundarban. *Environ. Sci. Pollut. Res Int* **26**, 9146–9160 (2019).
- Zhang, R., Yan, C. & Liu, J. Effect of mangroves on the horizontal and vertical distributions of rare earth elements in sediments of the Zhangjiang Estuary in Fujian Province, Southeastern China. *J. Coast. Res.* **29**, 1341–1350 (2013).

25. de Freitas, T. O. P., Pedreira, R. M. A. & Hatje, V. Distribution and fractionation of rare earth elements in sediments and mangrove soil profiles across an estuarine gradient. *Chemosphere* **264**, 128431 (2021).
26. Frank, M. Radiogenic isotopes: Tracers of past ocean circulation and erosional input. *Rev. Geophys.* **40**, 1–38 (2002).
27. Stichel, T. et al. Sources and input mechanisms of hafnium and neodymium in surface waters of the Atlantic sector of the Southern Ocean. *Geochim Cosmochim. Acta* **94**, 22–37 (2012).
28. van de Flierdt, T. et al. Global neodymium–hafnium isotope systematics — revisited. *Earth Planet Sci. Lett.* **259**, 432–441 (2007).
29. Lacan, F. & Jeandel, C. Neodymium isotopes as a new tool for quantifying exchange fluxes at the continent–ocean interface. *Earth Planet Sci. Lett.* **232**, 245–257 (2005).
30. Rahlf, P. et al. Tracing water mass mixing and continental inputs in the southeastern Atlantic Ocean with dissolved neodymium isotopes. *Earth Planet Sci. Lett.* **530**, 115944 (2020).
31. Stichel, T., Frank, M., Rickli, J. & Haley, B. A. The hafnium and neodymium isotope composition of seawater in the Atlantic sector of the Southern Ocean. *Earth Planet Sci. Lett.* **317**, 282–294 (2012).
32. Wang, R. et al. Reversible scavenging and advection – Resolving the neodymium paradox in the South Atlantic. *Geochim Cosmochim. Acta* **314**, 121–139 (2021).
33. Matos, C. R. L. et al. Seasonal changes in metal and nutrient fluxes across the sediment-water interface in tropical mangrove creeks in the Amazon region. *Appl. Geochem.* **138**, 105217 (2022).
34. Hollister, A. P., Leon, M., Scholten, J., Van Beek, P., Gledhill, M. & Koschinsky, A. Distribution and Flux of Trace Metals in the Amazon and Pará River Estuary and Mixing Plume. *Authorea*, <https://doi.org/10.1002/essoar.10512637.10512631> (2022).
35. Hollister, A. P. et al. Dissolved concentrations and organic speciation of copper in the Amazon River estuary and mixing plume. *Mar. Chem.* **234**, 104005 (2021).
36. de Carvalho, L. M., Hollister, A. P., Trindade, C., Gledhill, M. & Koschinsky, A. Distribution and size fractionation of nickel and cobalt species along the Amazon estuary and mixing plume. *Mar. Chem.* **236**, 104019 (2021).
37. Xu, A., Hathorne, E., Laukert, G. & Frank, M. Overlooked riverine contributions of dissolved neodymium and hafnium to the Amazon estuary and oceans. *Nat. Commun.* **14**, 4156 (2023).
38. Schneider, A. B., Koschinsky, A., Krause, C. H., Gledhill, M. & de Carvalho, L. M. Dynamic behavior of dissolved and soluble titanium along the salinity gradients in the Pará and Amazon estuarine system and associated plume. *Mar. Chem.* **238**, 104067 (2022).
39. Zieringer, M. The Hafnium and Neodymium Isotopic Composition of Surface Waters in the Tropical Atlantic Ocean. In: *GEOMAR Helmholtz Centre for Ocean Research Kiel*. University of Kiel (2011).
40. Sanders, C. J., Santos, I. R., Barcellos, R. & Silva Filho, E. V. Elevated concentrations of dissolved Ba, Fe and Mn in a mangrove subterranean estuary: Consequence of sea level rise? *Continental Shelf Res.* **43**, 86–94 (2012).
41. Thanh-Nho, N., Strady, E., Nhu-Trang, T. T., David, F. & Marchand, C. Trace metals partitioning between particulate and dissolved phases along a tropical mangrove estuary (Can Gio, Vietnam). *Chemosphere* **196**, 311–322 (2018).
42. de Lacerda, L. D., Ward, R. D., Borges, R. & Ferreira, A. C. Mangrove Trace Metal Biogeochemistry Response to Global Climate Change. *Frontiers in Forests and Global Change* **5**, (2022).
43. Knoke, M. et al. Outwelling of reduced porewater drives the biogeochemistry of dissolved organic matter and trace metals in a major mangrove-fringed estuary in Amazonia. *Limnol. Oceanogr.* **69**, 262–278 (2024).
44. Sholkovitz, E. R. The geochemistry of rare earth elements in the Amazon River estuary. *Geochim Cosmochim. Acta* **57**, 2181–2190 (1993).
45. Boyle, E., Edmond, J. & Sholkovitz, E. The mechanism of iron removal in estuaries. *Geochim Cosmochim. Acta* **41**, 1313–1324 (1977).
46. Elderfield, H. The oceanic chemistry of the rare-earth elements. *Philos. Trans. R. Soc. Lond. Ser. A, Math. Phys. Sci.* **325**, 105–126 (1988).
47. Bayon, G. et al. Environmental Hf–Nd isotopic decoupling in World river clays. *Earth Planet Sci. Lett.* **438**, 25–36 (2016).
48. Breithaupt J. L., Smoak J. M., Smith T. J., Sanders C. J. & Hoare A. Organic carbon burial rates in mangrove sediments: Strengthening the global budget. *Global Biogeochem. Cycles* **26**, (2012).
49. Tang, J. & Johannesson, K. H. Speciation of rare earth elements in natural terrestrial waters: assessing the role of dissolved organic matter from the modeling approach. *Geochim Cosmochim. Acta* **67**, 2321–2339 (2003).
50. Merschel, G., Bau, M. & Dantas, E. L. Contrasting impact of organic and inorganic nanoparticles and colloids on the behavior of particle-reactive elements in tropical estuaries: An experimental study. *Geochim Cosmochim. Acta* **197**, 1–13 (2017).
51. Tepe, N. & Bau, M. Behavior of rare earth elements and yttrium during simulation of arctic estuarine mixing between glacial-fed river waters and seawater and the impact of inorganic (nano-)particles. *Chem. Geol.* **438**, 134–145 (2016).
52. Kristensen, E., Bouillon, S., Dittmar, T. & Marchand, C. Organic carbon dynamics in mangrove ecosystems: A review. *Aquat. Bot.* **89**, 201–219 (2008).
53. Och, L. M. et al. Rare earth elements in the sediments of Lake Baikal. *Chem. Geol.* **376**, 61–75 (2014).
54. Holloway, C. J. et al. Manganese and iron release from mangrove porewaters: A significant component of oceanic budgets? *Mar. Chem.* **184**, 43–52 (2016).
55. Tachikawa, K., Toyofuku, T., Basile-Doelsch, I. & Delhay, T. Microscale neodymium distribution in sedimentary planktonic foraminifer tests and associated mineral phases. *Geochim Cosmochim. Acta* **100**, 11–23 (2013).
56. Otero, X. L. et al. Geochemistry of iron and manganese in soils and sediments of a mangrove system, Island of Pai Matos (Cananea — SP, Brazil). *Geoderma* **148**, 318–335 (2009).
57. Marchand, C. et al. The partitioning of transitional metals (Fe, Mn, Ni, Cr) in mangrove sediments downstream of a ferralitized ultramafic watershed (New Caledonia). *Chem. Geol.* **301**, 70–80 (2012).
58. Carpenter, D., Boutin, C., Allison, J. E., Parsons, J. L. & Ellis, D. M. Uptake and effects of six rare earth elements (REEs) on selected native and crop species growing in contaminated soils. *PLoS one* **10**, e0129936 (2015).
59. Rempfer, J., Stocker, T. F., Joos, F., Dutay, J.-C. & Siddall, M. Modelling Nd-isotopes with a coarse resolution ocean circulation model: Sensitivities to model parameters and source/sink distributions. *Geochim Cosmochim. Acta* **75**, 5927–5950 (2011).
60. Tachikawa, K., Athias, V. & Jeandel, C. Neodymium budget in the modern ocean and paleo-oceanographic implications. *J. Geophys. Res.* **108**, C8 (2003).
61. Gu, S. et al. Modeling Neodymium Isotopes in the Ocean Component of the Community Earth System Model (CESM1). *J. Adv. Modeling Earth Syst.* **11**, 624–640 (2019).
62. Arsouze, T., Dutay, J., Lacan, F. & Jeandel, C. Reconstructing the Nd oceanic cycle using a coupled dynamical-biogeochemical model. *Biogeosciences* **6**, 2829–2846 (2009).
63. Johannesson, K. H. & Burdige, D. J. Balancing the global oceanic neodymium budget: Evaluating the role of groundwater. *Earth Planet Sci. Lett.* **253**, 129–142 (2007).
64. Abbott, A. N., Haley, B. A. & McManus, J. Bottoms up: Sedimentary control of the deep North Pacific Ocean’s eNd signature. *Geology* **43**, 1035–1035 (2015).
65. Bunting P. et al. The Global Mangrove Watch—A New 2010 Global Baseline of Mangrove Extent. *Remote Sensing* **10**, 1669 (2018).

66. Goldberg, L., Lagomasino, D., Thomas, N. & Fatoyinbo, T. Global declines in human-driven mangrove loss. *Glob. Chang Biol.* **26**, 5844–5855 (2020).
67. Friess, D. A. et al. The State of the World's Mangrove Forests: Past, Present, and Future. *Annu. Rev. Environ. Resour.* **44**, 89–115 (2019).
68. Rao, K., Priya, N. & Ramanathan, A. L. Impact of seasonality on the nutrient concentrations in Gautami-Godavari Estuarine Mangrove Complex, Andhra Pradesh, India. *Mar. Pollut. Bull.* **129**, 329–335 (2018).
69. Adame, M. F., Virdis, B. & Lovelock, C. E. Effect of geomorphological setting and rainfall on nutrient exchange in mangroves during tidal inundation. *Mar. Freshw. Res.* **61**, 1197–1206 (2010).
70. Newell, R., Marshall, N., Sasekumar, A. & Chong, V. Relative importance of benthic microalgae, phytoplankton, and mangroves as sources of nutrition for penaeid prawns and other coastal invertebrates from Malaysia. *Mar. Biol.* **123**, 595–606 (1995).
71. Adame, M. F. & Lovelock, C. E. Carbon and nutrient exchange of mangrove forests with the coastal ocean. *Hydrobiologia* **663**, 23–50 (2011).
72. Lacerda, L. D., Ribeiro, M. G. & Gueiros, B. B. Manganese dynamics in a mangrove mud flat tidal creek in SE Brazil. *Mangroves Salt Marshes* **3**, 105–115 (1999).
73. Lacerda L. D. et al. Pluriannual Watershed Discharges of Hg into a Tropical Semi-Arid Estuary of the Jaguaribe River, NE Brazil. *J. Brazilian Chem. Soc.* **24**, 1719–1731 (2013).
74. Lacerda LDd, MarinsR. V. & Dias FJdS An Arctic Paradox: Response of Fluvial Hg Inputs and Bioavailability to Global Climate Change in an Extreme Coastal Environment. *Front. Earth Sci.* **8**, 93 (2020).
75. Twining, B. S. & Baines, S. B. The trace metal composition of marine phytoplankton. *Ann. Rev. Mar. Sci.* **5**, 191–215 (2013).
76. Huang, H., Gutjahr, M., Kuhn, G., Hathorne, E. C. & Eisenhauer, A. Efficient Extraction of Past Seawater Pb and Nd Isotope Signatures From Southern Ocean Sediments. *Geochem. Geophys. Geosyst.* **22**, e2020GC009287 (2021).
77. Gutjahr, M. et al. Reliable extraction of a deepwater trace metal isotope signal from Fe–Mn oxyhydroxide coatings of marine sediments. *Chem. Geol.* **242**, 351–370 (2007).
78. Elderfield, H. & Et, Sholkovitz Rare earth elements in the pore waters of reducing nearshore sediments. *Earth Planet Sci. Lett.* **82**, 280–288 (1987).
79. Bretschneider, L. et al. Provenance and Weathering of Clays Delivered to the Bay of Bengal During the Middle Miocene: Linkages to Tectonics and Monsoonal Climate. *Paleoceanogr. Paleoclimatol.* **36**, (2021).
80. Bayon, G. et al. Determination of rare earth elements, Sc, Y, Zr, Ba, Hf and Th in geological samples by ICP-MS after Tm addition and alkaline fusion. *Geostand. Geoanal. Res.* **33**, 51–62 (2009).
81. Pin, C. & Zalduogui, J. S. Sequential separation of light rare-earth elements, thorium and uranium by miniaturized extraction chromatography: application to isotopic analyses of silicate rocks. *Anal. Chim. Acta* **339**, 79–89 (1997).
82. Munker, C., Weyer, S., Scherer, E. & Mezger, K. Separation of high field strength elements (Nb, Ta, Zr, Hf) and Lu from rock samples for MC-ICPMS measurements. *Geochem. Geophys. Geosyst.* **2**, GC000183 (2001). 2001.
83. Vance, D. & Thirlwall, M. An assessment of mass discrimination in MC-ICPMS using Nd isotopes. *Chem. Geol.* **185**, 227–240 (2002).
84. Tanaka, T. et al. JNdi–1: a neodymium isotopic reference in consistency with LaJolla neodymium. *Chem. Geol.* **168**, 279–281 (2000).
85. Nowell, G. et al. High precision Hf isotope measurements of MORB and OIB by thermal ionisation mass spectrometry: insights into the depleted mantle. *Chem. Geol.* **149**, 211–233 (1998).
86. Jacobsen, S. B. & Wasserburg, G. Sm–Nd isotopic evolution of chondrites. *Earth Planet Sci. Lett.* **50**, 139–155 (1980).
87. Bouvier, A., Vervoort, J. D. & Patchett, P. J. The Lu–Hf and Sm–Nd isotopic composition of CHUR: Constraints from unequilibrated chondrites and implications for the bulk composition of terrestrial planets. *Earth Planet Sci. Lett.* **273**, 48–57 (2008).
88. Rahlf, P., Laukert, G., Hathorne, E. C., Vieira, L. H. & Frank, M. Dissolved neodymium and hafnium isotopes and rare earth elements in the Congo River Plume: Tracing and quantifying continental inputs into the southeast Atlantic. *Geochim Cosmochim. Acta* **294**, 192–214 (2021).
89. Sahoo, Y. V., Nakai, S. & Ali, A. Modified ion exchange separation for tungsten isotopic measurements from kimberlite samples using multi-collector inductively coupled plasma mass spectrometry. *Analyst* **131**, 434–439 (2006).
90. Taylor, S. R. & McLennan, S. M. *The continental crust: Its composition and evolution*. (Blackwell Scientific Pub. Palo Alto, CA 1985).
91. Schlitzer, R. Ocean data view. <https://odv.awi.de/> (2020).

### Acknowledgements

We thank the captain and crew of RV Meteor for their help and support during cruise M147. We also thank Jutta Heinze, Sieglinde Kolbrink, Marcus Gutjahr and Christopher Siebert for laboratory support and Lisa Bretschneider for sampling. We also acknowledge Alex Cabral for valuable advice on the Ra data calculation. The China Scholarship Council (CSC) is acknowledged for financial support of Antao Xu during this study. We gratefully acknowledge the permission granted by the Brazilian government (Ministério da Marinha) for the sampling conducted in this study.

### Author contributions

A.X., M.F., E.H. A.K. and T. D. designed and coordinated the study. M.F., E.H., M.S. and N.A. conducted the sampling. A.X. carried out the analytical work with guidance from E.H. T. L. conceptualized the predicted flux changes and helped with Ra data and flux calculations. A.X. wrote the manuscript. All coauthors contributed to the final version.

### Funding

Open Access funding enabled and organized by Projekt DEAL.

### Competing interests

The authors declare no competing interests.

### Additional information

**Supplementary information** The online version contains supplementary material available at <https://doi.org/10.1038/s43247-024-01989-1>.

**Correspondence** and requests for materials should be addressed to Antao Xu.

**Peer review information** *Communications Earth & Environment* thanks Raghav Ray and the other, anonymous, reviewer(s) for their contribution to the peer review of this work. Primary Handling Editors: Alice Drinkwater. A peer review file is available.

**Reprints and permissions information** is available at <http://www.nature.com/reprints>

**Publisher's note** Springer Nature remains neutral with regard to jurisdictional claims in published maps and institutional affiliations.

**Open Access** This article is licensed under a Creative Commons Attribution 4.0 International License, which permits use, sharing, adaptation, distribution and reproduction in any medium or format, as long as you give appropriate credit to the original author(s) and the source, provide a link to the Creative Commons licence, and indicate if changes were made. The images or other third party material in this article are included in the article's Creative Commons licence, unless indicated otherwise in a credit line to the material. If material is not included in the article's Creative Commons licence and your intended use is not permitted by statutory regulation or exceeds the permitted use, you will need to obtain permission directly from the copyright holder. To view a copy of this licence, visit <http://creativecommons.org/licenses/by/4.0/>.

© The Author(s) 2025